ARTICLE

Reorientable fluorinated aryl rings in triangular channel Fe-MOFs for CO_2 capture

Received 00th January 20xx,
Accepted 00th January 20xx

DOI: 10.1039/x0xx00000x

J. Perego, C. Bezuidenhout, A. Pedrini, S. Bracco, M. Negroni, A. Comotti* and P. Sozzani

The realization of tunable and functionalized MOFs is a winning strategy for CO_2 capture. Here we report on a series of robust Fe-MOFs with triangular channels constructed by rod-like fluorinated pyrazolate ligands, comprising an increasing number of fluorine atoms on the central *p*-phenylene core (F=1,2, and 4). This yielded a series of isoreticular frameworks, engineered with orientational flexibility of the fluorinated aryl rings pivoted on ethynyl groups with sp^2-sp soft rotary barrier, providing a stable axel, which supported reorientable C-F dipoles. A combined approach, including powder X-ray diffraction, multinuclear solid-state NMR (2D ^{1}H-^{13}C, ^{19}F, hyperpolarized ^{129}Xe NMR and distance measurements by paramagnetic shift), gas- adsorption and microcalorimetry enabled the exhaustive description of the fluorinated ring arrangement and the organization of functionalized sites for accommodating CO_2. In the tetrafluoro-aryl-derivative MOF protrusion of perfluorinated rings towards the channel space play a major role for CO_2 capture. Partially fluorinated aryl rings of mono- and di-fluoro MOFs turn to retract into the channel-walls to form continuous ribbons of inter-strut supramolecular interactions, contributing to the robustness of the overall architectures. Detailed computational models by GCMC and DFT of CO_2 diffusion and interactions in MOFs showed how the gas molecules approach the channel walls. The highly occupated sites are aligned at the corners of the triangular channels, wherein fluorine atoms participate in host-CO_2 interactions. CO_2-matrix adsorption enthalpy of 33 kJ/mol, suitable for capture/delivery cycles, was accurately measured *in-situ* by simultaneous acquisition of microcalorimetric and volumetric-isotherm data. Thus, the designed advantages of rotational flexible fluorinated moieties were successfully explored.

Introduction

The growing concentration of CO_2 in the atmosphere, as combustion product, has dramatic effects on the environment.[1] Since the transition to a complete use of renewable energy sources is still in the early stage, a concomitant reduction of CO_2 footprint of human activities is mandatory. A number of technologies, such as carbon capture and storage (CCS) and carbon capture and utilization (CCU), have been developed to reduce the CO_2 emissions.[2] However, CO_2 capture in power plants, which are one of the major contributors to the global CO_2 emissions, is still based on amine scrubbing technology, which suffers from the high costs and temperature conditions associated to adsorbent regeneration.[3] The need for an alternative approach to reduce the energy penalty associated with CO_2 capture advances the search for new materials with lower regeneration temperatures.

Porous materials such as metal–organic frameworks (MOFs), covalent organic frameworks (COFs), porous organic polymers (POPs) and porous molecular crystals (PMCs) have been reported as promising candidates for CO_2 capture and sequestration[4-15] since they contain voids inside their crystalline structures that can lead to high CO_2 uptakes, even under rather mild conditions. Porous materials give the possibility of tuning pore dimensions, functionalization, customized adsorption capacity and selectivity. Specifically, the rational choice of metal ions and ligands to self-assemble MOFs opens rich perspectives as efficient absorptive materials. MOF performances towards CO_2 adsorption have been optimized by the insertion of exposed metal sites, pre- or post-synthetic ligand modification and the creation of size-specific pores.[16]

Pyrazolates, thanks to their basicity and hapticity, provide a large variety of coordination modes[17,18] and enable the attainment of porous 3D frameworks.[19-21] The complexation of transition metals with pyrazole-based ligands affords strong coordination bonds, boosting both thermal and chemical stability, thus making these materials superior candidates for practical and industrial applications compared to their carboxylate-based analogues, that possess poorer stability in acidic or basic media.

The introduction of fluorine substituted ligands (i.e. F, CF_3) improves robusteness and performance under humid conditions, pivotal in real-life applications.[22,23] Fluorinated MOFs display good results as water-repellent and hydrocarbon adsorbers.[24] Regarding CO_2 capture, the presence of C-F dipoles in the structure can improve the host-gas interaction,[25,26] in particular, outstanding results were obtained in MOFs with fluorinated anions.[27,28]

Herein, a series of isoreticular fluorinated pyrazolate-based Fe-MOFs were constructed using long rod-like homologuos ligands

Dr. J. Perego, Dr. C. Bezuidenhout, Dr. A. Pedrini, Prof. S. Bracco, Dr. M. Negroni, Prof. A. Comotti and Prof. P. Sozzani
Department of Materials Science, University of Milano – Bicocca,
Via R. Cozzi 55, Milan, Italy.
Electronic Supplementary Information (ESI) available: [Sythesis, PXRD, Solid state NMR, Xe NMR, DFT and GCMC calculations]. See DOI: 10.1039/x0xx00000x

which support an increasing number of reorientable fluorine C-F dipoles on their para-phenylene core. Their non interpenetrated architectures with robust triangular channels were proved efficient in CO_2 sorption: the diverse orientation of the central fluorinated rings about the ligand main axis, yet permanently anchored in the frameworks, modulates the interaction energy. Indeed, the tailor-made design of the struts, composed by pivotal ethynyl extenders, provides torsional flexibility to the fluorinated para-phenylenes, enabling the systematic change of conformational arrangement within the strut in the 3D architectures. The isostructural series of Fe-MOFs provides a rare observation of CH--F interactions of the ligands aligned along the channel walls in the mono- and di-fluoroaryl-based compounds, in contrast to the protrusion of tetrafluoroaryl moieties into the channels in the tetrafluoro-based derivative. This led to dramatic consequences in intra-wall *vs* guest-wall interactions for CO_2 molecules diffusing into the channels. A multi-technique approach, which combines PXRD, solid state NMR including paramagnetic effect, hyperpolarized Xe NMR, microcalorimetry and computational models, provided a complete picture of the phenomenon. Remarkably, the CO_2 interaction strength with the host walls was evaluated by direct measurement of the heat evolved upon CO_2 adsorption using in-situ microcalorimetry-adsorption isotherm data acquisition. The adsorption enthalpy for the perfuorinated para-phenylene ring compound was as high as 33 kJ/mol, with moderate regeneration energy. Detailed computational simulations using GCMC and DFT of CO_2 diffusion and interactions in the MOFs show the preferential adsorption sites along the channel walls: in the corners of the triangular channels with cooperative fluorine interactions that stabilizes the CO_2 molecules.

Results and discussion

Three different bis(pyrazolate) linear struts bearing one, two (in adjacent positions) and four fluorine atoms on the central *p*-phenylene core were synthetized through Sonogashira coupling starting from 1,4-diethynyl-fluoroaryl derivatives and 4-iodio-(1-ethoxyethyl)pyrazole, followed by deprotection under acidic conditions.[29] The ethynyl groups were designed to bridge the terminal pyrazolate moieties that retain their coordination ability. The corresponding MOFs were prepared starting from the fluorinated ligands with Fe(III) salts under different reaction conditions with trimethylamine, thus generating crystalline materials (**Fe-PF1**, **Fe-PF2** and **Fe-PF4**, respectively) (Scheme 1 and Supporting Information). MOFs precipitated from the reaction medium as crystalline black powders, air stable and insoluble in water and the most common organic solvents. The microcrystalline powders were filtered and washed for a few times using fresh DMF followed by MeOH. The samples were activated at 150°C under dynamic vacuum overnight before further analyses.

Structural analysis

The fluorinated Fe-MOF structures were elucidated by the combination of DFT-based computational methods and Rietveld refinement of the PXRD patterns (Fig. S1-S3). The crystalline structures for the three compounds with an increasing number of fluorine atoms on the central *p*-phenylene ring **Fe-PF1, Fe- PF2** and **Fe- PF4** were solved in the orthorhombic space-group, *Fddd* (Fig. 1).

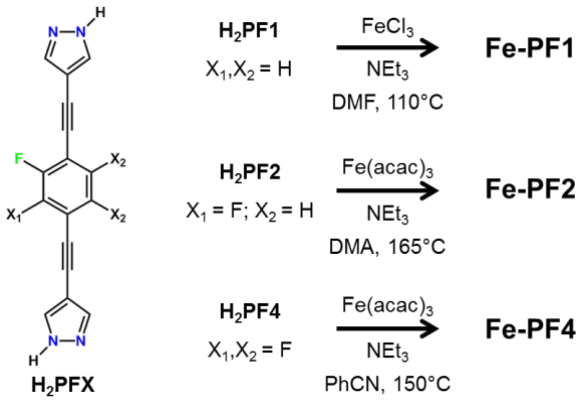

Scheme 1. Synthetic conditions for the preparation of the three fluorinated bis(pyrazolyl)-based MOFs.

The Fe(III) ions coordinate to six pyrazolate-nitrogen atoms in an octahedral coordination with consecutive bridging Fe(III) ions to form parallel 1-D columns with pyrazolate units (Fig. 1a). These bidentate bis(pyrazolate)-based ligands connect the columns into a three-dimensional porous framework. The structures display triangular 1-D channels with the faces defined by the ligands, while the the metal nodes occupy the edges.

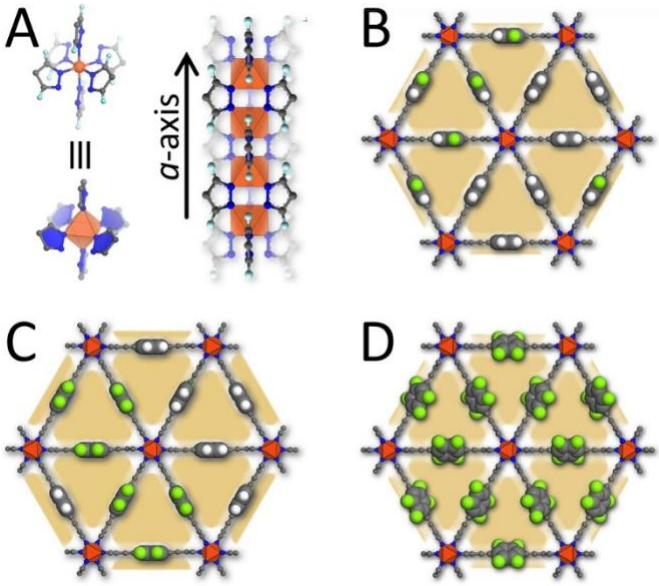

Figure 1. A) The Fe(III) octahedral coordination geometry (left) and the node propagation along the channel direction (right). B) – D) The crystal structures for **Fe-PF1**, **Fe-PF2** and **Fe-PF4**, respectively, shown along the channel axis (1 0 0). The metal coordination is shown in polygon representation, and the fluorinated moieties are shown in space-filling representation, while the rest is shown as ball-and-stick. The available space, mapped using a probe radius of 1.82 Å, is highlighted in light yellow. Hydrogen atoms that are not on the central rings have been omitted for clarity.

The cross-sectional areas of the triangular channels, determined from the guest-accessible volume calculated using a probe radius of 1.82 Å (kinetic diameter of N_2 is 3.64 Å), are 57, 60 and 57 $Å^2$ for **Fe-PF1, Fe-PF2** and **Fe-PF4,** respectively. These values are equivalent to

a circular diameter of 8.5-8.7 Å, which agrees with the pore size distribution centered at 8 Å calculated from N_2 adsorption isotherms at 77 K (see below). In **Fe-PF1, Fe-PF2** the planes of the aryl groups are aligned along the channel axis, while in the **Fe-PF4** the perfluorinated aromatic moieties are visibly rotated protruding towards the inner channel.

The channel cross-section is defined by three ligands: the main axis of one ligand is arranged perpendicular to the channel axis while the other two are tilted to an angle of ca. 82° (Fig. 2a-c). On each face of the channel, the ligands are parallel to one another and separated by 7.5 Å for **Fe-PF1** and **Fe-PF2** and 8.1 Å for **Fe-PF4** (Fig. 2g-i).

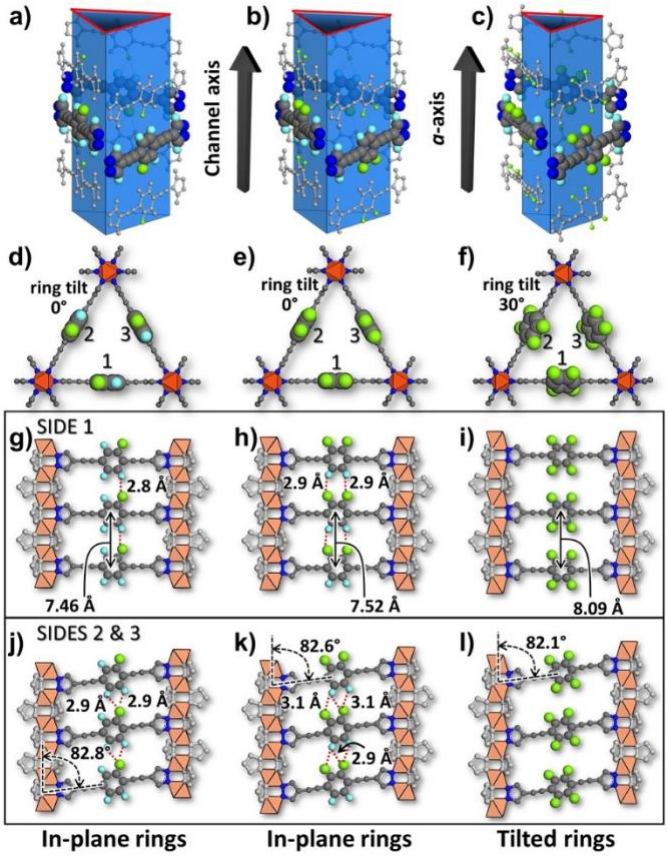

Figure 2. (a) **Fe-PF1**, (b) **Fe-PF1** and (c) **Fe-PF1**, a perspective view of the triangular channels of all three MOFs and the arrangement of their respective ligands around these channels. Single triangular channels of **Fe-PF1** (d), **Fe-PF2** (e) and **Fe-PF4** (f) viewed along (1 0 0), the channel axis, with the fluorinated rings in space-filling representation. The tilt of phenyl rings about the ligand axis is shown and the three sides of the triangular channels are indicated by 1, 2 and 3. A face-on view of side 1 of the channel walls for **Fe-PF1** (g), **Fe-PF2** (h) and **Fe-PF4** (i) showing the ligand-ligand (L--L) distance. A face-on view of sides 2 and 3 of the channel walls for **Fe-PF1** (j), **Fe-PF2** (k) and **Fe-PF4** (l) showing the angle between (ca. 82°) the ligand axis and the *a*-axis (channel axis). The red dotted lines indicate the hydrogen bonds formed by the ligands (Ls) along with their respective F---H distances. The ligands are shown in ball-and-stick while the metal coordination nodes are shown in polyhedron representation. The peripheral pyrazole moieties are shown in light grey and non-relavant hydrogens have been removed for clarity.

In the case of mono and difluoro-based MOFs such a distance allows for the coplanarity of the central fluorinated rings within the same face (Fig. 2d,e) and the formation of effective C-H···F intermolecular interactions with distances as short as 2.8/2.9 Å (Fig. 2g,h).[30] Thus, the walls are decorated by an infinite layer of cooperative C-H···F interactions and generate a head-to-tail alignment of the C-F dipoles. Contrarily, in **Fe-PF4** the absence of hydrogens on the perfluorinated ring and the steric hindrance between fluorine atoms on adjacent ligands force the aryl moieties to tilt toward the channels (Fig. 2f). Interestingly, the ability of the central rings to reorient with respect to the channel axis based on the number of fluorine atoms is owed to the torsional flexibility of the pivotal Csp-Csp^2 bonds of the fluorinate *p*-phenylene ring.

The thermal behavior of the fluorinated MOFs was investigated by thermogravimetric analysis (TGA). The TGA runs, performed in air, show high stability up to 300 - 350 °C (Fig. S11-S13). The absence of weight-loss events related to solvent release indicates the effective activation of samples. The MOFs retain their crystal structure after soaking in H_2O for 24 hours: the PXRD pattern was completely reproduced, as reported in Fig. S14, showing the high stability of the MOFs under humid conditions.

Solid state NMR is a method of choice to depict purity and connectivity of porous materials.[31,32] Specifically, monodimensional ^{1}H, ^{1}H-^{13}C, ^{19}F-^{13}C CP and two-dimensional ^{1}H-^{13}C MAS NMR experiments were applied to Fe-MOF samples, which demonstrated solvent free materials that are neither amorphous nor contain uncoordinated pyrazole groups (Fig. 3). Notably, the peculiar feature of the present structure is that the juxtaposition of Fe^{3+} atoms regularly spaced in the crystal structure produced systematic paramagnetic shifts of the carbon resonances along the rod-like ligands, according to the distances from the iron nodes (pseudocontact shift $\propto 1/r^3$).[33] In fact, ^{13}C{^{1}H} and ^{13}C{^{19}F} CP MAS spectra, performed both with and without cross polarization, highlighted the expansion of the total spectral width over a much wider range (ca. 200 ppm) than that of the free ligand (ca. 85 ppm), which is unaffected by the interactions with the paramagnetic ion (Fig. 3A,B, S17). The spectral expansion, by the large paramagnetic shift, helps distinguish the crowded signals of unsaturated nuclei along the ligand with the increasing influence from the central ring to the ends of the struts. Thus, the presence of the paramagnetic ion was beneficial to distinguish the crowded signals of the pure ligand. Additionally, the efficient cross-polarization from ^{19}F to ^{13}C nuclei offers a different observatory, e.g. the carbon atoms covalently linked or in proximity of the fluorine, allowing us to undoubtedly recognize the carbon atoms of the central fluorinated aryl core (Fig. S17). In the case of **Fe-PF2**, while the resonances of the aromatic core (C7) remained substantially unaffected, the ethynyl (C3) and pyrazolate (C2) carbons show ???42 and ???105 ppm upfield shifts, respectively, producing signals at ?=49 and ?=-2 ppm, since they are subjected to the effect of two Fe(III) ions symmetrically arranged at distances of 5.4 and 4.2 Å, respectively (Fig. 3D). Pyrazolate (C1) carbon appears at a chemical shift as low as ?=-50 ppm, with a 185 paramagnetic upfield shift, under the strong influence of a 2.9 Å proximity with Fe^{+3} ion. The entity of the shifts is consistent with solid state NMR spectra reported for Fe^{+3} in proteins and hemoglobin.[34]

ARTICLE

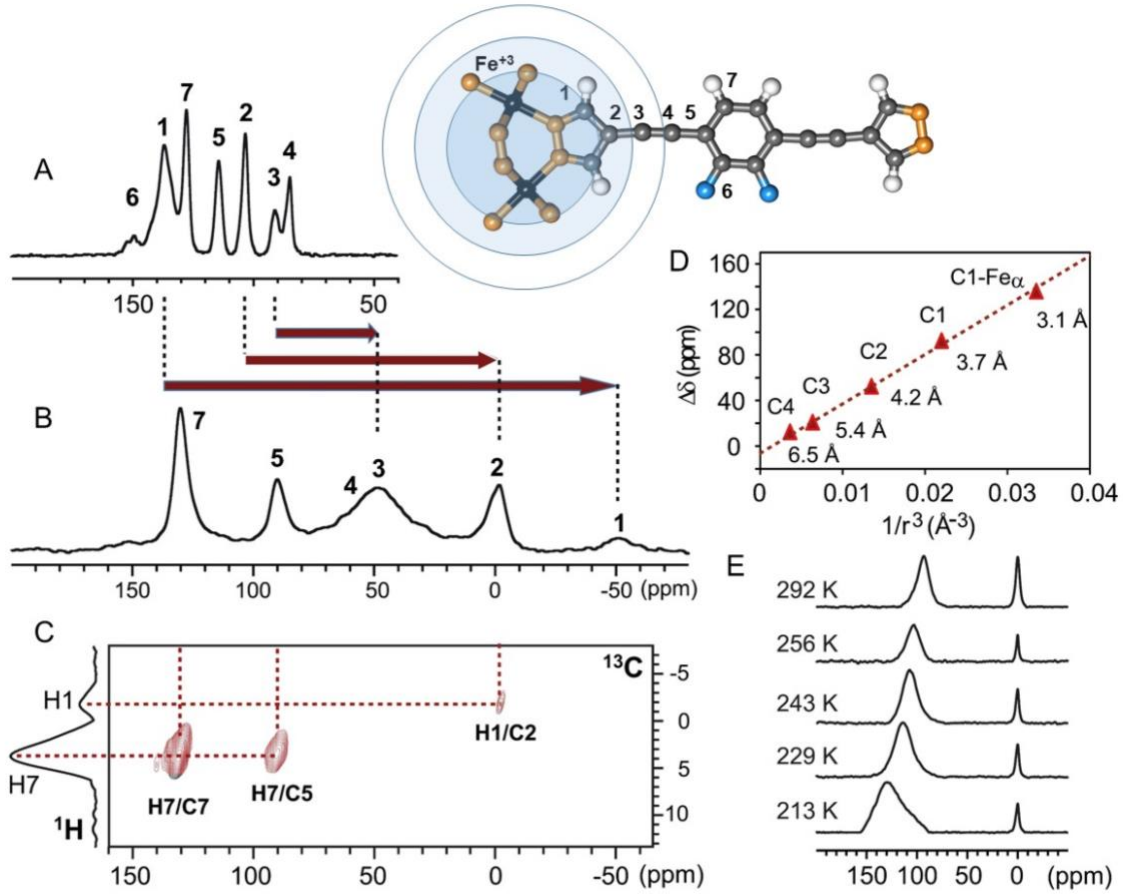

Figure 3. A) $^{13}C\{^{1}H\}$ CP MAS NMR spectrum of **H_2-PF2**. In the inset the ligand coordinated to Fe^{+3} ions as arranged in the crystal structure; the spheres of influence of paramagnetic effect onto the observed nuclei at increasing radii. B) $^{13}C\{^{1}H\}$ CP MAS NMR spectrum of **Fe-PF2** with a contact time of 2 ms. The arrows show the remarkable upfield shift due to the presence of the paramagnetic species. C) 2D ^{1}H-^{13}C HETCOR MAS NMR spectrum showing the correlation peaks between the ^{1}H and ^{13}C nuclei. D) Linear dependence of the ^{13}C pseudocontact paramagnetic shift per Fe ion *vs* the reciprocal of cube of the distance. The upfield shift for C1 is reported with respect to the average of the distance cube between the two Fe ion. C1-Fe$_{\square}$ indicates the shift of C1 from the closest Fe ion (Table S5). The distances between carbons and Fe ion are reported. E) Hyperpolarized ^{129}Xe NMR of the gas flowing in the channels of **Fe-PF2** at different temperature.

This is a rare case of the use of paramagnetic elements for elucidating the crystal structure of MOFs, in a similar way "shift-reagents" expand the spectral range in a regioselective manner.[35] 2D ^{1}H-^{13}C correlated NMR spectrum of difuoro-based derivative allows for the neat distinction of the core hydrogen from the pyrazolate hydrogen (Fig. 3C,S21), in fact hydrogen H7 on the fluorinated ring is slightly influenced by paramagnetic iron, while hydrogen H1 undergoes an impressive upfield shift ⍰⍰ of 10 ppm (Fig. S19) and is manifested in through-space magnetization transfer to the neighbour C1. Indeed, the non-protonated carbons receive magnetization from non-bonded ^{1}H nucleus, thus substantiating the assignments.

A complementary point of view is provided by ^{129}Xe NMR spectroscopy, by which the spin-active xenon gas collects information from the cavities it explores. A challenging method of the experiment is the laser-induced production of a continuous flow of hyperpolarized xenon after magnetization exchange with Rb in the gas phase.[36-38] Once flowed to the magnet, xenon reports immediately on the porosity of the sample at high sensitivity, even when diluted at 2% concentration. The chemical shift of ^{129}Xe in a confined system is much different from that of

^{129}Xe in the gas phase, which is considered the reference zero. Indeed, in **Fe-PF2** ^{129}Xe signal resonates at □93 ppm at room temperature (Fig. 3E). At the diluted limit, the Xe-probe samples the interaction with the surrounding surface, with the advantage that the Xe–Xe interactions become negligible. Under these conditions the chemical shift □$_s$, due solely to interactions with the surfaces, depends on the mean free path L that defines the size of the explored micropores as □$_s$ = 243*2.054/(2.054 + L), according to a semiempirical model proposed by Fraissard.[39,40] Taking into account the xenon diameter (4.4 Å), the pore size accessible to xenon atoms in the Fe-MOF was evaluated as 7.7 Å. This is consistent with pore size from N_2 adsorption isotherm at 77 K of 8 Å from a cylindrical model (see later on). Lowering the temperature, there is a downfield shift due to the increased residence time of xenon on the internal surfaces. This behavior is similar to the middle-size pore zeolites as NaY.[41] GCMC simulations show that Xe atoms are mainly localized in proximity of the channel walls and especially at the corners, as clamped between two pyrazolate moieties (Fig. S22). Interestingly, the ^{129}Xe response can be obtained after a period of time as short as 200 ms, indicating the open nature of the channels and the fast diffusion kinetics of the gas.

Gas Adsorption

The permanent porosity of the homologous MOFs was demonstrated by N_2 adsorption-desorption measurements at 77 K (Fig. S26-28). The N_2 adsorption isotherms display Type I profiles, which is characteristic of microporous solids. The absence of hysteresis on adsorption-desorption isotherms is characteristic of an open pore structure, as expected by the presence of channels inside the MOF frameworks. The main textural parameters of the three materials are reported in Table S7. The Langmuir surface areas account for 1610, 1660 and 1645 m^2/g with pore volumes of 0.70, 0.67 and 0.71 cm^3/g for **Fe-PF1**, **Fe-PF2 and Fe-PF4,** respectively. The pore size distribution is centered at 8 Å, as calculated by NLDFT method using the Tarazona cylindrical pore model, in agreement with the values calculated from the crystal structures and from Xe NMR chemical shift. CO_2 adsorption isotherms at 195 K show a similar type-I behaviour with a comparable saturation value of 120 moelcules per unit-cell (MPU) at p/p°=0.95, corresponding to 66% by weight. The CO_2 adsorption profiles can be successfully modelled by GCMC simulations, which confirm the Langmuir behaviour and the CO_2 loading capacity. In the low-pressure limit the adsorption behaviour differs remarkably in the three compounds and shows that the tetrafluorobenzene-based compound isotherm runs far above those of **Fe-PF1** and **Fe-PF2**, both in the experimental and simulated isotherms. This is a first indication that the number of fluorine atoms play a role in increasing the CO_2-matrix affinity. Moreover, CO_2 isotherms were collected at three distinct temperatures (273 K, 283 K and 298 K) up to 10 bar (Fig. 4). The adsorption capacity reaches the value of 57% by weight at 10 bar and under the mild conditions of 273 K, this value corresponds to 86% of the saturation value. The adsorption capacities at 273 K and 1 bar are of 5.1 (22.4%), 6.2 (27.3%) and 5.3 mmol/g (23.3%) for **Fe-PF1, Fe-PF2** and **Fe-PF4**, respectively.

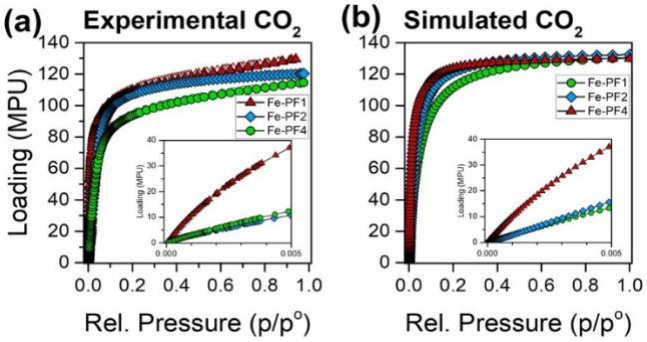

Figure 3. The experimental (a) and simulated (b) CO_2 adsorption isotherms at 195 K for **Fe-PF1** (green circles), **Fe-PF2** (blue diamonds) and **Fe-PF4** (red triangles). The insets expand the region from 0 – 0.005 p/p° and 0 – 40 molecules per unit-cell (MPU).

The best performance is shown by **Fe-PF2** which, to date, outperforms most of MOFs with fluorinated ligands, except for TKL-107.[42-48] Under the mild conditions of 298 K and 1 bar, it adsorbs 3.2 mmol/g (14% by weight), thus outperforming several MOFs including SNU-50, MOF-505, MOF-5, PCN-61, UiO-66 and IRMOF-74 functionalized with alkylamino groups.[16,49] N_2 adsorption isotherms from 273 K to 298 K show a much lower adsorption capacity than those for CO_2, suggesting an efficient selectivity in favour of CO_2, as calculated by Ideal Adsorbed Solution Theory (IAST) (Fig. S31).

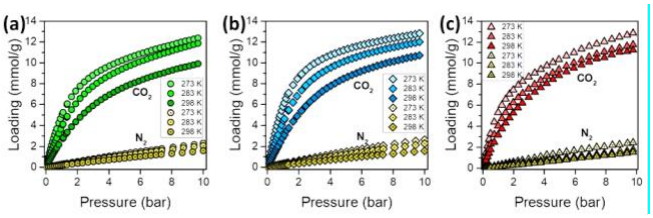

Figure 4. a) – c) CO_2 adsorption isotherms collected at 273 K, 283 K and 298 K up to 10 bar for **Fe-PF1** (green circles), **Fe-PF2** (blue diamonds) and **Fe-PF4** (red triangles). N_2 adsorption isotherms collected at 273 K, 283 K and 298 K up to 10 bar is shown in yellow for all three MOFs. The lighter colour represents the low temperature while the darker colour the high temperatures.

In-situ CO_2-matrix microcalorimetry

We applied a hyphenated technique which couple volumetric adsorption analyser with a gas-solid microcalorimeter, enabling the simultaneous detection of both gas loading and heat evolution at 293 K (Fig 5a,5c). The adsorption enthalpy ΔH_{ads} is determined from the heat evolved during each pressure increment and the associated gas loading for each increment (Fig. 5). This method allows a reliable measurement of the heat with high accuracy and precision, overcoming critical issues and approximations of multiple temperature experiments: in particular, it is valid also in the presence of phase transitions or significant guest-guest interactions.[50] The experimental set-up and data process was validated on a well-known reference

compound HKUST-1 (Fig. S32-S34).[51] The Q_{st} curves determined from microcalorimetry yielded at low coverage 28 kJ/mol for **Fe-PF1**, **Fe-PF2** and 33 kJ/mol for **Fe-PF4** (Fig. 5d). The most energetic interaction of 33 kJ/mol was noticed for the MOF with the highest number of fluorine atoms: the value is comparable to PCN-624,[46] dptz-Cu-SIF6[52] and SIFSIX-2-Cu-i[27] and overcomes the fluorinated MOFs with the same number of fluorine atoms on the *p*-phenylene ring, i.e. UiO-66(Zr)-F4 and UiO-66(Ce)-F4.[47,48]

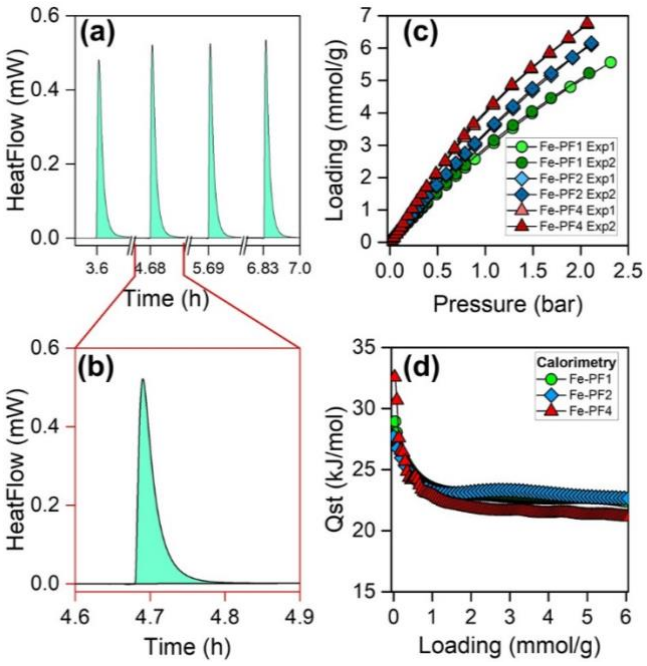

Figure 5. a) A small segment of the heat flow measurement of the CO_2 adsorption for **Fe-PF1** using the sorption and high-pressure µDSC coupled system collected at 293 K up to 2 bar. Each peak represents a gas dose and an adsorption point (See ESI for full-scale plots). b) An expanded timeline of 4.6 – 4.9 hours highlighting the peak shape of a single adsorption dose. c) The corresponding CO_2 adsorption isotherms collected with the coupled system for **Fe-PF1** (green circles), **Fe-PF2** (blue diamonds) and **Fe-PF4** (red triangles). The symbols with and without the dot represent the duplicate experiments pairs. d) Q_{st} plots calculated from the micro-calorimetry data collected at 293 K up to 2 bar, for **Fe-PF1** (green circles), **Fe-PF2** (blue diamonds) and **Fe-PF4** (red triangles). The errors for both a) and c) are given in the ESI.

Computational analysis of CO_2

The effect of the fluorinated ligand arrangements on the intermolecular interactions with diffusing-in CO_2 was investigated by Gran Canonical Monte Carlo (GCMC) simulations and Density Functional Theory (DFT) calculations. The CO_2 distribution density map at low loading (1 CO_2 molecule per unit cell) reflects the shape and symmetry of the triangular channel (Fig. 6a and S44-S46). The maximum probability of CO_2 occupation is concentrated in close proximity to the corners in all compounds. In the case of **Fe-PF4**, the high probability areas (red) are in closer proximity to the channel walls compared to **Fe-PF1** and **Fe-PF2**, owing more favorable interactions with the fluorinated rings protruding toward the channels. DFT calculations unveiled the favorable arrangements of CO_2 in the interaction sites at the corners of the channel (Fig. 6b and S49). One of the CO_2 oxygen atoms interacts simultaneously with two hydrogens belonging to pyrazolate groups of consecutive ligands within the same channel face, achieving CH--O distances as short as 2.4-2.9 Å with both hydrogens, i.e. at the van der Walls contacts. Only in **Fe-PF4** does the CO_2 carbon atom approach the fluorine atom of the tilted aryl group more closely and yields a close contact of 3.0 Å, thus installing a third interaction that further stabilizes the CO_2 in the specific site (Fig. 6b). Short distances in specific sites between CO_2 and fluorinated moieties have been observed in MOFs such as dptz-CuTiF6.[52] The calculated interaction energy between CO_2 and the interacting ligands in the triangular corner is 28.4 kJ/mol for **Fe-PF4**, in agreement with the experimental value. Moreover, the electrostatic potential calculations,[53-55] projected onto the CO_2 density isosurface (Fig. 6c,6d), confirm the complementarity of electrostatic charges of the quadrupolar CO_2 with those of the ligands (O_{CO2}--$H_{pyrazolate}$ and C_{CO2}--F_{aryl} groups). The structural arrangement of the central perfluorinated aryl group oriented toward the channel and the cooperative effect of the pyrazolate CH and aryl CF groups toward CO_2 molecules provide the explanation for the higher enthalpy in the **Fe-PF4**, as measured by microcalorimetry. Thus, the efficient CO_2 uptake and low regeneration energy combined with thermal and chemical stability makes these fluorinated MOFs good candidates for carbon capture.

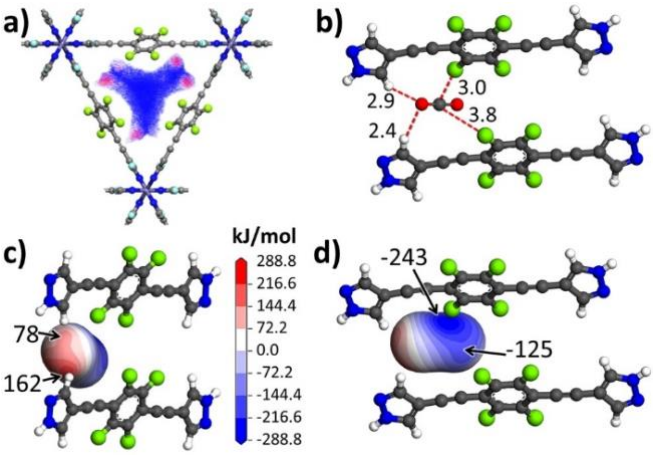

Figure 6. a) The CO_2 distribution density at low loading as viewed along the channel axis, within **Fe-PF4,** calculated using GCMC simulations. The red and blue colors represent high and extremely low CO_2 density, respectively. b) The CO_2 localized in the channel as determined by plane-wave DFT optimizations with a few key distances indicated by the red dotted lines. c) and d) The electrostatic potential of the **PF4** ligands projected onto the CO_2 density isosurface shown with perspective views of the CO_2 molecule to highlight the main interactions with the **PF4** ligands.

Conclusions

Collectively, a few florinated MOFs with triangular channels were constructed, with the final aim to compare their gas sorption

properties. The originality of the strategy lies in the creation of isostructural frameworks, with the systematic variation of fluorine numbers, from 1 to 4, inserted in the core of the struts. This was made possible by the design of a long rod-like axel, which connects in series organic moieties with specialized functions. The fluorinated central rings in the ligand do not modify the frameworks significatively, which retain their triangular shape channels, but can rotate for finding their preferential arrangement of C-F dipoles in the distinct MOFs. From the structural point of view the comparison among the fluorinated MOFs is intriguing: tetrafluoro-derivative displays a tilt of the fluorinated-substituted rings, which spring into the channel, while mono- and di-substituted compounds engage CH--F hydrogen interactions along the channel walls, forming flat layers of aromatic groups.

CO_2 sorption and interactions with the crystalline matrices could be therefore identified in relation to fluorine atom arrangements in the retailed void spaces through the direct comparison. The role performed by fluorine atoms was shown to be an interplay among structural configurations and interactions. Nevertheless, an interaction energy of 33 kJ/mol, suitable for efficient loading/delivery cycles, was exhibited in the case of tetrafluoro-derivative, substantiating the synergy of the number of fluorine atoms on the ligand and the suitable orientation of the C-F bonds. This is an indication that orientational flexibility within the pore walls, realized here, affords the fluorinated fragments sufficient degree of freedom to find the most suitable geometry with approaching gas molecules. This conceptual advancement can be of some utility and extended to other systems, provided the intra-wall interactions do not prevail.

Rare direct observations of the fast gas uptake and accessibility of the channels were demonstrated by hyperpolarized Xe NMR. Additionally, adsorption enthalpy was measured by an instrumental set-up, which exploits stepwise gas loadings with simultaneous detection of volumetric adsorption isotherm and calorimetric evolved heat: this method was useful in consolidating the interactions of the gas both with the pore walls and in the presence of already confined gas at high loading. Thus, these two techniques provided a direct measurement of the parameters required to define the industrial operative conditions. Indeed, the development of high-capacity robust fluorinated MOF structures with Fe(III) stimulates practical applications, in view of their notable stability to heat and water exposure.

Conflicts of interest

There are no conflicts to declare.

Acknowledgements

Financial support from the Italian Ministry of University and Research (MIUR) through grant “Dipartimenti di Eccellenza- 2017 "Materials For Energy” is gratefully acknowledged. This work was supported by the Ministry of Education, University and Research (PRIN grant n. 20173L7W8K). The authors would like to thank A. Maspero for helpful discussions.

Notes and references

1 P. Friedlingstein, et al., *Earth Syst. Sci. Data*, 2019, **11**, 1783-1838.
2 D. M. Reiner, Nat. Energy, 2016, **1**, 1-7.
3 P. Markewitz, W. Kuckshinrichs, W. Leitner, J. Linssen, P. Zapp, R. Bongartz, A. Schreiber and T. E. Müller, *Energy Environ. Sci.*, 2012, **5**, 7281-7305.
4 Y. Belmabkhout, V. Guillerm and M. Eddaoudi, *Chem. Eng. J.*, 2016, **296**, 386-397.
5 K. Adil, Y. Belmabkhout, R. S. Pillai, A. Cadiau, P. M. Bhatt, A. H. Assen, G. Maurinb and M. Eddaoudi, *Chem. Soc. Rev.*, 2017, **46**, 3402-3430.
6 H. S. Scott, N. Ogiwara, K.-J. Chen, D. G. Madden, T. Pham, K. Forrest, B. Space, S. Horike, J. J. Perry IV, S. Kitagawa and M. J. Zaworotko *Chem. Sci.*, 2016, **7**, 5470-5476.
7 H. Li, K. Wang, Y. Sun, C. T. Lollar, J. Li and H. C. Zhou, *Mater. Today*, 2018, **21**, 108–121.
8 S. Das, P. Haesman, T. Ben and S. Qiu, *Chem. Rev.*, 2017, **117**, 1515–1563.
9 R. Dawson, A. I. Cooper and D. J. Adams, *Prog. Polym. Sci.*, 2012, **37**, 530–563.
10 H. Wang, Z. T. Zeng, P. Xu, L. S. Li, G. M. Zeng, R. Xiao, Z. Y. Tang, D. L. Huang, L. Tang, C. Lai, D. N. Jiang, Y. Liu, H. Yi, L. Qin, S. J. Ye, X. Y. Ren and W. W. Tang, *Chem. Soc. Rev.*, 2019, **48**, 488 -516.
11 H. Furukawa and O. M. Yaghi, *J. Am. Chem. Soc.*, 2009, **131**, 8875–8883.
12 Neil B. McKeown, *Polymers of Intrinsic Microporosity*. ISRN Materials Science. 2012, 1. doi:10.5402/2012/513986
13 I. Bassanetti, S. Bracco, A. Comotti, M. Negroni, C. Bezuidenhout, S. Canossa, P. P. Mazzeo, L. Marchio and P. Sozzani, *J. Mater. Chem. A*, 2018, **6**, 14231–14239.
14 G. Xing, I. Bassanetti, S. Bracco, M. Negroni, C. Bezuidenhout, T. Ben, P. Sozzani and A. Comotti, *Chem. Sci.*, 2019, **10**, 730-736.
15 N. B. Mckeown, *J. Mater. Chem. A*, 2010, **20**, 10588-10597.
16 T. M. McDonald, W. Ram Lee, J. A. Mason, B. M. Wiers, C. S. Hong and J. R. Long, *Chem. Rev.*, 2012, **112**, 724-781.
17 S. Trofimenko, in: S. J. Lippard (Ed.), *Progress in Inorganic Chemistry*, vol. 34, Wiley, 1986, pp.115-220.
18 R. Mukherjee, *Coord. Chem. Rev.*, 2000, **203**, 151-218.
19 K. T. Mercedes, T. Runcevski, J. Oktawiec, M. I. Gonzalez, R. L. Siegelman, J. A. Mason, J. Ye, C. M. Brown and J. R. Long, *J. Am. Chem. Soc.*, 2016, **138**, 15019-15026.
20 S. Galli, A. Maspero, C. Giacobbe, G. Palmisano, L. Nardo, A. Comotti, I. Bassanetti, P. Sozzani and N. Masciocchi, *J. Mater. Chem A*, 2014, **2**, 12208–12221.
21 C. Giacobbe, E. Lavigna, A. Maspero and S. Galli, *J. Mater. Chem. A*, 2017, **5**, 16964–16975.
22 S.-I. Noro and T. Nakamura, *NPG Asia Materials*, 2017, **9**, e433.
23 P. Pachfule and R. Banerjee, in *Encyclopedia of Inorganic and Bioinorganic Chemistry*, John Wiley & Sons, Ltd., 2014, pp. 1-124.
24 C. Yang, U. Kaipa, Q. Z. Mather, X Wang, V. Nesterov, A. F. Venero and M. A. Omary, *J. Am. Chem. Soc.*, 2011, **133**, 45, 18094-18097.
25 C. E. Wilmer, O. K. Farha, Y.-S. Bae, J. T. Hupp and R. Q. Snurr, *Energy Environ. Sci.*, 2012, **5**, 9849-9856.
26 A. Comotti, F. Castiglioni, S. Bracco, J. Perego, A. Pedrini, M. Negroni and P. Sozzani, *Chem. Comm.*, 2019, **55**, 8999-9002.
27 P. Nugent, Y. Balmabkhout, S. D. Burd, A. J. Cairns, R. Luebke,K. Forrest, S. Ma, B. Space, L. Waoitas, M. Eddaoudi and M. J. Zaworotko, *Nature*, 2013, **495**, 80–84.

28 Y. Belmabkhout, P. M. Bhatt, K. Adil, R. S. Pillai, A. Cadiau, A. Shkurenko, G. Maurin, G. Liu, W. J. Koros and M. Eddaoudi, *Nature Energy*, 2018, **3**, 1059-1066

29 K. Sonogashira, Y. Tohda, and N. Hagihara, *Tetrahedron Lett.*, 1975, **16**, 4467-4470.

30 Jack. D. Dunitz and W. Bernd Schweizer *Chem. Eur. J.* 2006, **12**, 6804-6815.

31 A. Comotti, S. Bracco, P. Sozzani, S. Horike, R. Matsuda, J. Chen, M. Takata, Y. Kubota and S. Kitagawa *J. Am. Chem. Soc.*, 2008, **130**, 13664-13672.

32 A. Comotti, S. Bracco and P. Sozzani, Solid-State NMR of Supramolecular Materials, in Comprehensive Supramolecular Chemistry II, Ed. Chiefs: J. Atwood, Eds: G. W. Gokel and L. Barbour, Elsevier, 2017, pp. 75-99.

33 D. Joss and D. Häussinger, in *Progr. in Nuclear Magnetic Resonance Spectroscopy*, 2019, **114-115**, 284-312.

34 H. Fujii, *J. Am. Chem. Soc.*, 1999, **121**, 3818-3828.

35 T. C. Morrill, *Lanthanide Shift Reagents in Stereochemical Analysis,* 1986, VCH, New York.

36 P. Sozzani, S. Bracco and A. Comotti, in *Porous Materials Explored by Hyperpolarized Xenon NMR*, New Developments in NMR No. 4, Hyperpolarized Xenon-129 Magnetic Resonance: Concepts, Production, Techniques and Applications, , Ed. T. Meersmann and E. Brunner, The Royal Society of Chemistry, 2015, 164-184.

37 P. Sozzani, A. Comotti, R. Simonutti, T. Meersmann, J. W. Logan and A. Pines, *Angew. Chem. Int. Ed.*, 2000, **39**, 2695-2699.

38 A. Comotti, S. Bracco, L. Ferretti, M. Mauri, R. Simonutti and P. Sozzani, *Chem. Comm.*, 2007, 350-352.

39 J. Demarquay and J. Fraissard, *Chem. Phys. Lett.*, 1987, **136**, 314-318.

40 P. Sozzani, S. Bracco, A. Comotti, M. Mauri, R. Simonutti and P. Valsesia, *Chem. Comm.*, 2006, 1921-1923.

41 C. J. Jameson, *J. Am. Chem. Soc.*, 2004, **126**, 10450-10456.

42 A. M. Cheplakova, K. A. Kovalenko, D. G. Samsonenko, V. A. Lazarenko, V. N. Khrustalev, A. S. Vinogradov, V. M. Karpov, V. E. Platonov and V. P. Fedin, *Dalt. Trans.*, 2018, **47**, 3283–3297.

43 A. Buragohain, S. Couck, P. Van Der Voort, J. F. M. Denayer and S. Biswas, *J. Solid State Chem.*, 2016, **238**, 195–202.

44 H.-H.a Wang, T.-T. Guo, D. Xie, Z.-Q. Bai, L. Hou, and Y.-Y. Wang, *Eur. J. Inorg. Chem.*, 2015, 5773–5780.

45 D.-S. Zhang, Z. Chang, Y.-F. Li, Z.-Y. Jiang, Z.-H. Xuan, Y.-H. Zhang, J.-R. Li, Q. Chen, T.-L. Hu and X.-H. Bu, *Sci. Rep.*, 2013, **3**, 3312-

46 N. Huang, K. Wang, H. Drake, P. Cai, J. Pang, J. Li, S. Che, L. Huang, Q. Wang and H. C. Zhou, *J. Am. Chem. Soc.*, 2018, **140**, 6383–6390.

47 R. D'Amato, A. Donnadio, M. Carta, C. Sangregorio, D. Tiana, R. Vivani, M. Taddei, and F. Costantino, *ACS Sustain. Chem. Eng.*, 2019, **7**, 394−402.

48 Z. Hu, A. Gami, Y. Wang, and D. Zhao, *Adv. Sustain. Syst.*, 2017, **1**, 1700092.

49 Y. Lin, C. Kong, Q. Zhang and L. Chen, *Adv. Energy Mater.*, 2017, **7**, 1601296 (1-29).

50 W. K. Feldmann, K.-A. White, C. X. Bezuidenhout, V. J. Smith, C. Esterhuysen and L. J. Barbour, *ChemSusChem*, 2020, **13**, 102-105.

51 S. S. Y. Chui, S. M. F. Lo, J. P. H. Charmant, A. G. Orpen, I. D. Williams, *Science*, 1999**, 283**, 1148-1150.

52 W. Liang, P. M. Bhatt, A. Shkurenko, K. Adil, G. Mouchaham, H. Aggarwal, A. Mallick, A. Jamal, Y. Belmabkhout and M. Eddaoudi, *Chem.*, 2019, **5**, 950–963

53 J. S. Murray and P. Politzer, *WIREs Computational Molecular Science*, 2011, **1**, 153-163.

54. C. X. Bezuidenhout, V. J. Smith, P. M. Bhatt, C. Esterhuysen and L. J. Barbour, *Angew. Chem. Int. Ed.*, 2015, **54**, 2079-2083.

55. E. R. Engel, V. J. Smith, C. X. Bezuidenhout and L. J. Barbour, *Chem. Comm.*, 2014, **50**, 4238-4241.

